Magn Reson Med Sci 2020; 19; 108–118
doi:10.2463/mrms.mp.2019-0015
Published Online: May 10, 2019

MAJOR PAPER

Comparison of q-Space Reconstruction Methods for Undersampled Diffusion Spectrum Imaging Data

Gabriel E. Varela-Mattatall[1,2,3], Alexandra Koch[4], Rüdiger Stirnberg[4], Steren Chabert[5], Sergio Uribe[1,3,6,7], Cristian Tejos[1,2,3], Tony Stöcker[4,8], and Pablo Irarrazaval[1,2,3,7*]

Purpose: To compare different q-space reconstruction methods for undersampled diffusion spectrum imaging data.

Materials and Methods: We compared the quality of three methods: Mean Apparent Propagator (MAP); Compressed Sensing using Identity (CSI) and Compressed Sensing using Dictionary (CSD) with simulated data and *in vivo* acquisitions. We used retrospective undersampling so that the fully sampled reconstruction could be used as ground truth. We used the normalized mean squared error (NMSE) and the Pearson's correlation coefficient as reconstruction quality indices. Additionally, we evaluated two propagator-based diffusion indices: mean squared displacement and return to zero probability. We also did a visual analysis around the centrum semiovale.

Results: All methods had reconstruction errors below 5% with low undersampling factors and with a wide range of noise levels. However, the CSD method had at least 1–2% lower NMSE than the other reconstruction methods at higher noise levels. MAP was the second-best method when using a sufficiently high number of q-space samples. MAP reconstruction showed better propagator-based diffusion indices for *in vivo* acquisitions. With undersampling factors greater than 4, MAP and CSI have noticeably more reconstruction error than CSD.

Conclusion: Undersampled data were best reconstructed by means of CSD in simulations and *in vivo*. MAP was more accurate in the extraction of propagator-based indices, particularly for *in vivo* data.

Keywords: *compressed sensing, diffusion propagator, diffusion spectrum imaging, mean apparent propagator, q-space reconstruction*

Introduction

Diffusion, at a microscopic level, consists of molecules' random displacements given a diffusion time Δ. This set of possible displacements, **r**, has associated a probability density function (PDF), $p(\mathbf{r}|\Delta)$, which is the so-called diffusion propagator.[1] The reconstruction of the diffusion propagator is relevant to describe the complete diffusion process and to extract biomarkers without any assumption of the microstructure.

Diffusion MRI is a technique that estimates the diffusion propagator for each imaging voxel. Usually, T_2-weighted images are made sensitive to diffusion by including diffusion encoding gradients, with amplitude $|\mathbf{G}|$ and duration δ, that are separated by the diffusion time Δ. Thus, these images contain the effect of diffusion in the direction of **G** over Δ.[2] The data acquired in q-space, $\mathbf{q} = \delta\mathbf{G}\gamma/2\pi$, correspond to the Fourier transform of the diffusion propagator. The direct reconstruction of the center-of-mass[3] diffusion propagator from the magnitude of the complete q-space data is called diffusion spectrum imaging (DSI).[4,5] Further details and recent improvements for DSI acquisition and reconstruction can be found in Lacerda et al.,[6] Paquette et al.,[7] and Tian et al.[8]

[1]Biomedical Imaging Center, Pontificia Universidad Católica de Chile, Santiago, Chile
[2]Department of Electrical Engineering, Pontificia Universidad, 4860 Vicuna Mackenna, Macul, Católica de Chile, Santiago 782-0436, Chile

Received: January 29, 2019 | Accepted: March 21, 2019

[3]Millennium Nucleus for Cardiovascular Magnetic Resonance, Santiago, Chile
[4]German Center for Neurodegenerative Diseases (DZNE), Bonn, Germany
[5]Department of Biomedical Engineering, Universidad de Valparaíso, Valparaíso, Chile
[6]Radiology Department, Pontificia Universidad Católica de Chile, Santiago, Chile
[7]Institute for Biological and Medical Engineering, Pontificia Universidad Católica de Chile, Santiago, Chile
[8]Department of Physics and Astronomy, University of Bonn, Bonn, Germany
*Corresponding author, Phone: +56-2235-44292, E-mail: pim@uc.cl

The DSI reconstruction for each voxel is defined as Eq. [1]

$$p(\mathbf{r}) = \int_{\mathcal{R}^3} \left| E(\mathbf{q}) \right| e^{i2\pi \mathbf{qr}} \; d\mathbf{q}, \qquad [1]$$

where $p(\mathbf{r})$ is the diffusion propagator given the fixed diffusion time for a traditional q-space acquisition and $E(\mathbf{q})$ are the values of the q-space samples. The Fourier transform for DSI requires a minimum q-space sampling to fulfill the Nyquist criterion. Since each q-space sample is a diffusion-weighted scan, the DSI acquisition becomes time-expensive for clinical settings.

When the full diffusion propagator is not needed, model-based methods are suitable to compute specific diffusion indices. Typically, the propagator is approximated by the diffusion tensor model. Even though diffusion tensor imaging (DTI)[9] has shown relevance in clinical applications,[10,11] this approximation may not describe correctly, or completely, the tissue microstructure. For example, DTI provides a biased result, if the voxel contains two or more non-parallel fibers.[12] Another model technique is diffusion kurtosis imaging (DKI)[13] that incorporates the non-Gaussian diffusion using the kurtosis parameter. Unfortunately, DKI cannot be used in a complete q-space regime due to high signal to noise ratio requirements. A discussion on models in diffusion MRI and their assumptions can be found in Hagmann et al.,[14] Assemlal et al.,[15] and Ferizi et al.[16]

On the other hand, compressed sensing (CS)[17] has been used to fully reconstruct the diffusion propagator from undersampled q-space data. CSI uses as prior knowledge that the data should be represented sparsely in some domain. The first publication of CS in DSI[18] proposed to use total variation and Haar wavelets as sparse domains. Soon after, Bilgic et al.[19] proposed to use a data-driven dictionary as sparse domain. This method had around 1.6-fold improvement in reconstruction quality, measured as the normalized mean squared error (NMSE) when compared with;[18] however, that work lacked simulations to describe in a more controlled environment the performance and limitations of both methods. Recently, Paquette et al.[20] proposed a joint improvement by selecting the Cohen–Daubechies–Feauveau 9/7 wavelet as sparse domain; and a sparse undersampling pattern using a uniform angular distribution with randomly allocated samples along radial profiles. That work analyzed most of the commonly used sparsifying transforms such as wavelets, total variation and the identity basis from Menzel et al.,[18] Bilgic et al.,[19] Merlet;[21] and different undersampling patterns as in Menzel et al.[18] However, a comprehensive comparison between CS-based reconstruction methods with reconstruction methods that fit the q-space signal to a highly efficient set of continuous basis functions is yet to be done. A representative method using continuous basis functions is the mean apparent propagator (MAP),[22,23] a method which approximates the diffusion propagator using Hermite functions. The first basis function corresponds to the diffusion tensor as in DTI and the rest characterize any deviation from DTI. Up to some extent, MAP has a better characterization of q-space than other continuous basis functions because it takes advantage of the anisotropic nature of its scaling tensor, whereas other methods that use isotropic scaling would require more basis functions to obtain the same reconstruction quality.[24]

In this work, we compared the methods of MAP, Compressed Sensing using Identity (CSI) as sparsifying transform and Compressed Sensing using Dictionary (CSD). The novelty of this comparison is that we included MAP in addition to CSI and CSD methods, which were previously analyzed in Bilgic et al.[19] and Paquette et al.[20]

Materials and Methods

The three reconstruction methods were tested using retrospectively undersampled q-space data from Monte-Carlo simulations and from an *in vivo* brain acquisition. The reconstructions were compared with the fully sampled data as ground truth to evaluate reconstruction quality and retrieval of propagator-based diffusion indices. Finally, the *in vivo* reconstructions were used for a visual analysis of the centrum semiovale.

Data sets

Simulations and *in vivo* data were done in an 11 × 11 × 11 q-space Cartesian grid. Each complete data set had 257 q-space samples contained in a discrete half-sphere with a radius of five samples. The other half was obtained by symmetry.

For the Monte-Carlo simulations, we used the crossing substrate from the Camino software.[25,26] The substrate corresponds to two fiber populations in interleaved planes and one population was rotated with respect to the other population to resemble two crossing fiber bundles with a certain crossing angle. The fiber populations were done with a cylinder radius of 2 μm and a cylinder separation of 5.1 μm. We used 10^3 time steps for 10^5 spins, initially uniform-distributed, to diffuse in the crossing substrates. We simulated two crossing fibers with crossing angles in [0, 15, 30, … 90]°. The diffusion encoding parameters for the simulations were with δ = 31 ms and Δ = 43.2 ms, where q_{max} = 62.21/mm^2 (or b_{max} = 6600 s/mm^2); and TE = 88 ms. Gaussian noise was added to the real and imaginary part of the simulated measurements to obtain Rician noise in the magnitude of the diffusion signal as $E(\mathbf{q})_i = \sqrt{(E_{\text{simulation}}(\mathbf{q}) + \eta_{i,1})^2 + \eta_{i,2}^2}$, where $\eta_{i,1}$, $\eta_{i,2} \sim N(0, \sigma)$ and standard deviation σ = 1/SNR.[20] For simulations, σ was chosen as [0, 1, 2, …, 10]% of the peak value. Each noisy experiment was repeated fifty times. The ground truth for simulations were the inverse Fourier transform of the noise-free and fully sampled measurements, $F^{-1}\{E_{\text{simulation}}(\mathbf{q})\}$.

For the *in vivo* acquisition, we used fully sampled DSI acquisitions collected as in Tobisch et al.[27] Data were acquired in a 3T Prisma scanner (Siemens Healthcare, Erlangen, Germany) at 1.5 mm isotropic resolution (TE/TR = 105/6100 ms, b_{max} = 6800 s/mm^2, Δ = 51.3 ms, δ = 20.1 ms) using a 64-channel head–neck coil. A total of 257 diffusion

weighted and eight interleaved, non-weighted images were acquired with both anterior-to-posterior and posterior-to-anterior phase encoding. Finally, the acquired data were processed in FMRIB Software Library (FSL) to estimate and correct for susceptibility geometric distortions, eddy currents and subject motion.[28,29] The total scan time was 55 min. The ground truth for *in vivo* data were the inverse Fourier transform of the fully sampled q-space from each voxel.

The fully sampled data from simulations and acquisitions were retrospectively undersampled from 2× to 8× to test reconstruction performance. The sampling pattern was a 3D Cartesian q-space grid where the central 3 × 3 × 3 samples were always sampled and the rest, depending on the undersampling factor (USF), were picked randomly with a variable decreasing density distribution.[18,19]

We repeated the reconstructions with ten different sampling patterns using the previously mentioned strategy to establish if the reconstruction quality was invariant to both, the microstructure orientation and the particular sampling pattern. To test dependency on the angle between undersampling pattern and fiber orientation, we also reconstructed simulations (as described above) of a single fiber with USF = 4, and noise = 5% rotated in a plane using [0, 15,…,165]°.

Reconstruction

The reconstruction methods are as follows.

Mean apparent propagator

Mean apparent propagator[22,23] is a least-squares optimization that finds the best fit to q-space data as Eq. [2],

$$\hat{\mathbf{c}} = \text{argmin}_{\mathbf{c}} \left\| S\boldsymbol{\Phi}(\mathbf{A},\mathbf{q})^{\mathrm{T}}\mathbf{c} - E(\mathbf{q}) \right\|_2^2 \ \text{s.t} \ \ \boldsymbol{\Psi}(\mathbf{A},\mathbf{q})^{\mathrm{T}}\mathbf{c} \geq 0, \quad [2]$$

where $\mathbf{c}$ are the coefficients to estimate, $\boldsymbol{\Phi}(\mathbf{A}, \mathbf{q})^{\mathrm{T}}$ is the basis in q-space and $\boldsymbol{\Psi}(\mathbf{A}, \mathbf{q})^{\mathrm{T}}$ is the corresponding basis in PDF-space. Each basis function from $\boldsymbol{\Phi}$ and $\boldsymbol{\Psi}$ are scaled by $\mathbf{A} = \text{diag}(\mu_1^2, \mu_2^2, \mu_3^2)$, where $\mu_{\{1,2,3\}} = \sqrt{2\lambda_{\{1,2,3\}}\tau}$ is the square root of the mean displacement for each eigenvalue of the diffusion tensor, which was fitted to all q-space measurements. Because of the eigendecomposition of the diffusion tensor, each 3D basis function in $\boldsymbol{\Phi}$ is the combination of three 1D orthogonal basis functions, $\phi_n(\mu, q)$, where each one of them corresponds to the n-th order Hermite polynomial, H_n, modulated by a Gaussian-like term. The 1D basis function is defined as Eq. [3]

$$\phi_n(\mu, q) = \frac{1}{i^n\sqrt{2^n n!}} \exp\left(-\frac{(2\pi\mu q)^2}{2}\right) H_n(2\pi\mu q). \quad [3]$$

An interesting property of $\phi_n(\mu, q)$ is that its Fourier transform also results in a Gauss–Hermite function, $\psi_n(\mu, r)$, as

$$\psi_n(\mu, r) = \frac{1}{\mu\sqrt{2^{n+1}\pi n!}} \exp\left(-0.5\left(\frac{r}{\mu}\right)^2\right) H_n\left(\frac{r}{\mu}\right); \quad [4]$$

and this is the 1D basis function that generates each 3D basis function for $\boldsymbol{\Psi}$. Furthermore, $\boldsymbol{\Phi}$ and $\boldsymbol{\Psi}$ share the same coefficients, so it is possible to optimize data consistency while imposing properties of the diffusion propagator like non-negativity. Therefore, the first basis function ($n = 0$) in $\boldsymbol{\Phi}$ and $\boldsymbol{\Psi}$ correspond to Gaussian diffusion whereas the remaining basis functions ($n > 0$) correspond to non-Gaussian diffusion. The bases $\boldsymbol{\Phi}$ and $\boldsymbol{\Psi}$ were constructed as in Özarslan et al.[22] and according to recommendations from Avram et al.[23] Hence, we used a maximum basis order of six, $N_{\max} = 6$, which corresponds to the first 50 basis functions from the truncated infinite series. The number of basis functions is defined by the following expression [5]:

$$\boldsymbol{\Phi}(\mathbf{A}, \mathbf{q}) = \sum_{N=0}^{N_{\max}} \sum_{\substack{i,j,k>0 \\ i+j+k=N}} \phi_i(\mu_1, q_1)\phi_j(\mu_2, q_2)\phi_k(\mu_3, q_3), \quad [5]$$

to ensure that all the possible combinations for the respective maximum basis order are included to design both bases, $\boldsymbol{\Phi}$ and $\boldsymbol{\Psi}$. For symmetric signals, only even values of N are non-zero; therefore, the number of basis functions is defined by $B(N_{\max}) = (N_{\max} + 2)(N_{\max} + 4)(2N_{\max} + 3) / 24$. Finally, in this work, the diffusion propagator from MAP was obtained as $\hat{p}(\boldsymbol{r}) = F^{-1}\{\boldsymbol{\Phi}(\mathbf{A},\mathbf{q})^{\mathrm{T}}\hat{\boldsymbol{c}}\}$.

Compressed sensing

Compressed sensing is a method that imposes sparsity in the representation of the diffusion propagator while maintaining data consistency (Eq. [6]):

$$\hat{p}(\boldsymbol{r}) = \text{argmin}_{p(r)} \frac{1}{2}\left\| SFp(\boldsymbol{r}) - E(\boldsymbol{q}) \right\|_2^2 + \lambda \left\| \Omega p(\boldsymbol{r}) \right\|_1. \quad [6]$$

Data consistency ensures the similarity between the estimation and the acquired data $E(\mathbf{q})$, where SF is the undersampled Fourier operator. The regularization constrains $p(\mathbf{r})$ to be represented sparsely in the domain Ω. For the data sets in this work, we used $\Omega = I$ since it is suitable and computationally efficient.[19,20] Finally, the optimization was done using a non-linear conjugate gradient implementation. The parameter λ was empirically fixed according to the procedure explained in Appendix A.

CS using data-driven dictionaries

CS using data-driven dictionaries is a CSI reconstruction that obtains the diffusion propagator by fitting coefficients to a trained dictionary.[19] The method iteratively solves:

$$\begin{aligned} W_{j,j}^t &= \text{diag}\left(\left|x_j^t\right|^{\frac{1}{2}}\right) \\ \boldsymbol{s}^t &= \text{argmin}_s \,||\, s \,||_2^2 \text{ such that } SF\,\mathbf{D}\mathbf{W}^{\mathrm{t}}\boldsymbol{s} = E(\mathbf{q}), \\ \boldsymbol{x}^{t+1} &= \mathbf{W}^t\mathbf{s}^t \end{aligned} \quad [7]$$

where $\mathbf{D}$ is the dictionary obtained from a training set of diffusion propagators using the K-SVD algorithm.[30] The idea of this dictionary is to sparsely concentrate the variance between

propagators in the first k-th atoms from the dictionary. $\mathbf{W}^t$ is a diagonal weighting matrix whose j-th diagonal entry is denoted $W^t_{j,j}$ and this matrix multiplied with s^t equals $\mathbf{X}^{t+1}$, which are the corresponding coefficients after the last iteration t. The focal underdetermined system solver promotes l_1-sparsity on the coefficients $\mathbf{X}^{t+1}$ through reweighted l_2-optimizations on the auxiliary variable s^t. For more information see Ye et al.[31] Implementation was downloaded from Berkin Bilgic web site (http://martinos.org/~berkin/software.html).

For the simulation case, the training was done with simulated noise-free single fibers rotated across the three axes in the PDF-space. For this purpose, we simulated in Camino single fibers using a wide range of diameters and separation between cylinders. The experiments were done using this dictionary, but with simulations of two crossing fibers (as described above). For the *in vivo* case, the training was done with propagators from fully-sampled q-space data of one axial slice. The *in vivo* training was done as in Bilgic et al.[19] The reconstruction was performed along a coronal slice to avoid a bias in favor of the CSD method. The particular axial slice used for training the dictionary was removed from the comparison. The diffusion propagator was obtained as $\hat{p}(\boldsymbol{r}) = \mathbf{D}\mathbf{x}^{t+1}$.

Finally, in all reconstruction methods, the negative values found in each diffusion propagator were clipped to zero.[7]

Quality indices and visualization

To compare the reconstruction $\hat{p}$ against the ground truth p, we used the normalized mean squared error, $\mathrm{NMSE}\{\hat{p}, p\} = \hat{p} - p_2^2 / p_2^2$, and the Pearson's correlation (PC) coefficient.[20] We also compared two propagator-based diffusion indices: the mean squared displacement (MSD)[32] and the return to zero probability ($p0$).[22,33] The MSD is the second moment of the PDF and the relative MSD error was defined as $\Delta\mathrm{MSD}(\hat{p}, p) = (\mathrm{MSD}\{\hat{p}\} - \mathrm{MSD}\{p\})^2 / \mathrm{MSD}\{p\}^2$. The relative return to zero probability error was defined as $\Delta p0\{\hat{p}, p\} = (p0\{\hat{p}\} - p0\{p\})^2 / p0\{p\}^2$.

The *in vivo* reconstructions were loaded into DSI Studio (http://dsi-studio.labsolver.org) to visually analyze the orientational information from the reconstructions around the centrum semiovale. This region contains the intersection of multiple white matter bundles; therefore, it is a complex area in the brain suitable to evaluate multiple crossing angles.[8]

Results

Simulations

Figure 1 shows the mean and standard deviation of the NMSE index for the reconstructions of a single fiber rotated at [0, 15,…,165]° in a plane with USF = 4. Figure 1a shows that the reconstructions were slightly biased for angles aligned with the Cartesian grid (0° and 90°), i.e. the reconstructions are not entirely independent of the microstructure orientations. This result agrees with what was obtained in Lacerda et al.,[6] where it is stated that the orientation distribution function reconstruction depends on q-space acquisition and resolution. Figure 1b shows a slice of the sampling pattern. To avoid this orientational bias between the Cartesian grid and the orientation from simulations, we rotated the noise-free simulations by $\pi/4$ in the three axes.

Figure 2 shows the mean and standard deviation of the NMSE and PC indices (50 reconstructions) of two crossing fibers while varying noise level, USF and crossing angle. Both reconstruction quality indices are consistent, ranking the methods in the order: CSD, MAP, and CSI. Figure 2a depicts NMSE as a function of noise. At σ = 5%, NMSE obtained with MAP and CSI were 1.1- and 1.5-fold higher than the NMSE from CSD; which agrees with the results in Bilgic et al.[19] The same behavior can be seen in Fig. 2d for the PC. Figure 2b depicts NMSE as a function of USF and it shows that the CSD method performed better than the other methods for USF above 4×; which again agrees with Bilgic et al.[19] Between 2× and 8×, the mean NMSE from CSD increased around 2% while MAP and CSI mean NMSE increased around 8% and 5% respectively. This is also shown for PC in Fig. 2c and 2e depicts NMSE as a function of the crossing angle. The ranking of reconstructions is preserved and it is worth mentioning the increased error from CSI at lower crossing angles. More prominent Gibbs ringing were observed at small crossing angles, which may be an explanation for the increased errors. Furthermore, resolving small crossing angles is generally known to be challenging, even with advanced diffusion MRI, which may as well explain increased NMSE values.

The previous results were reproduced for nine additional undersampling patterns to verify whether these results were influenced by the selection of the specific sampling pattern.

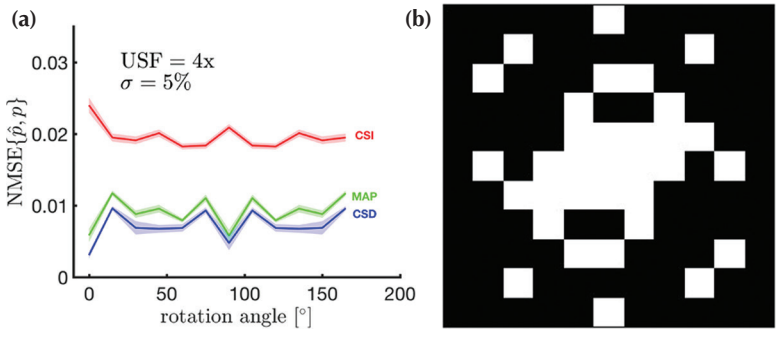

Fig. 1 Effect of the fiber orientation in the reconstruction of a single fiber rotated over in pdf-space. The NMSE as a function of the rotation angle in (**a**) shows that the reconstructions were slightly biased for rotation angles aligned with the Cartesian grid (0º and 90º). The corresponding central plane of the 3D q-space sampling pattern at 4× is shown in (**b**) as reference. NMSE, normalized mean squared error; USF, undersampling factor; CSI, Compressed Sensing using Identity; MAP, Mean Apparent Propagator; CSD, Compressed Sensing using Dictionary.

Although there is a natural variance from randomized patterns, the ranking of the reconstruction methods was preserved and most of them agree quantitatively too, which can be seen in Appendix B.

Figure 3 shows the mean and standard deviation of the propagator-based relative index errors as functions of noise, undersampling and crossing angle from the reconstructions of crossing fibers. Figure 3a and 3d show almost exact recovery (error below 2%) of the index as a function of noise. Furthermore, Fig. 3a demonstrates that CSI may provide the best relative MSD error even at a relatively high USF of 4, if the noise level is relatively low ($\sigma \leq 4\%$). Figure 3b and 3e show that both indices suffer considerably for USF above 4× in the cases of CSI and MAP. Figure 3c depicts the relative MSD error as a function of the crossing angle and it shows that the relative MSD obtained from CSI has around a 2% error with respect to the ground truth. This may indicate that at USF = 4, CSI reconstruction is obtaining

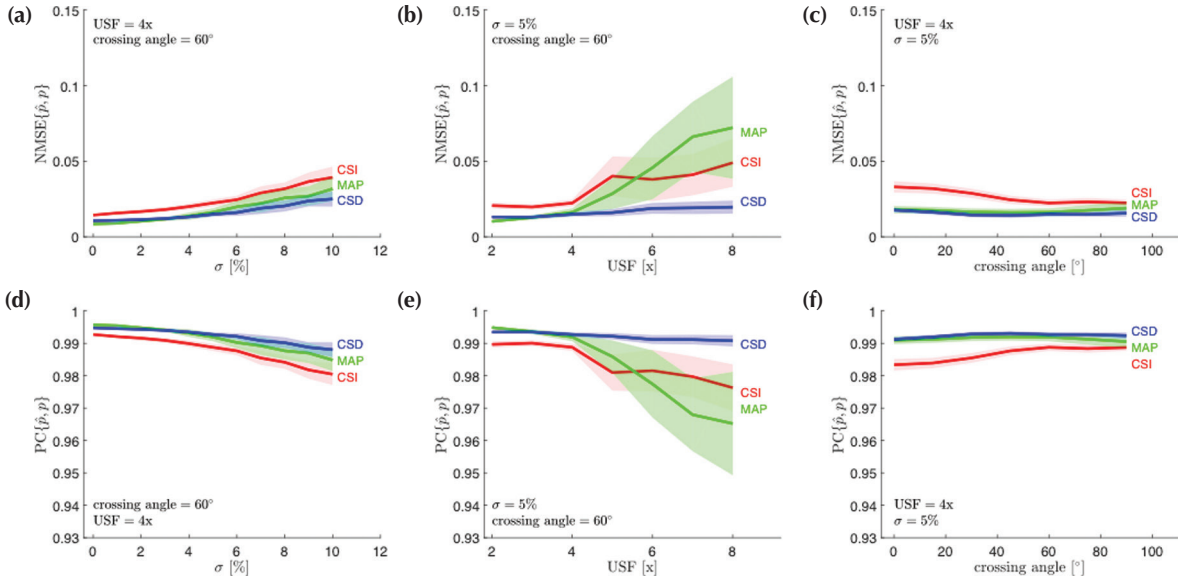

Fig. 2 Reconstruction quality indices for different settings from simulations of two crossing fibers. The first row corresponds to NMSE as a function of noise level σ (**a**); as a function of USF (**b**); and as a function of crossing angle (**c**). The second row corresponds to PC as a function of the same variables (**d–f**). USF, undersampling factor; NMSE, normalized mean squared error; PC, Pearson's correlation coefficient; CSI, Compressed Sensing using Identity; MAP, Mean Apparent Propagator; CSD, Compressed Sensing using Dictionary.

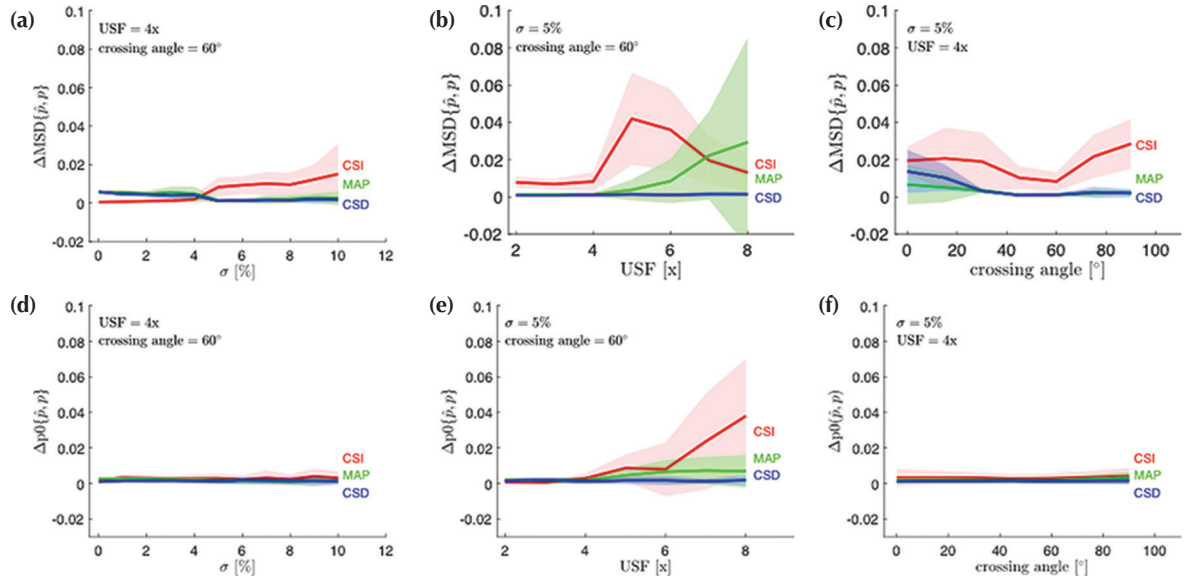

Fig. 3 Error metrics for propagator-based diffusion indices for different settings from simulations of two crossing fibers. The first row corresponds to relative MSD error as a function of noise level σ (**a**); as a function of USF (**b**); and as a function of crossing angle (**c**). The second row corresponds to relative $p0$ error as a function of the same variables (**d–f**). MSD, mean squared displacement; $p0$, return to zero probability; USF, undersampling factor; CSI, Compressed Sensing using Identity; MAP, Mean Apparent Propagator; CSD, Compressed Sensing using Dictionary.

a close approximation of the shape, but not an exact recovery of the ground truth which slightly influences the retrieval of the MSD index. Finally, Fig. 3f shows an excellent estimation of $p0$ for all crossing angles.

In vivo *data*

Figure 4 shows spatial maps of NMSE, (1-PC), relative MSD error and relative $p0$ error for the reconstruction methods using USF = 4 along a coronal slice. For visual clarity the PC coefficient has been subtracted from one, i.e. lower values indicate greater correlation to the ground truth. The axial slice used to train the dictionary of the CSD method was removed from the comparison (red line). In general terms, the three methods show reconstruction quality below 5% error; except in areas containing cerebrospinal fluid or deep brain areas. On the other hand, the methods show high reconstruction quality for the corticospinal tract, the corpus callosum and the corona radiata in comparison with other regions. Additionally, reconstruction quality indices indicate a correlation with the signal-to-noise ratio (SNR) which, for small parallel imaging factors and hence negligible geometry factors, can be assumed to be linked to the receive coil sensitivity map (decreasing toward the center of the brain). With regard to the estimation of the relative MSD and relative $p0$ errors, the MAP reconstruction shows higher quality when compared with CSI and CSD methods. We included the spatial maps of NMSE for the three reconstruction methods using USF = 4–6, and 8 in Appendix C.

Finally, Fig. 5 shows the generalized fractional anisotropy maps from the ground truth and the reconstruction methods under investigation. From each map, we zoomed the region around the centrum semiovale for visual inspection of the directional information from the propagators obtained for those voxels. All methods show high similarity with the ground truth, but there are areas where directional information has errors (see for example the upper left corner of the zoomed areas).

Discussion

In this work, three methods to reconstruct the diffusion propagator from undersampled q-space data were compared. These methods were MAP, CSI (Compressed Sensing using Identity as sparsifying transform) and CSD (Compressed Sensing using data-driven dictionaries for sparse representation). The comparison was done in terms of the reconstruction quality

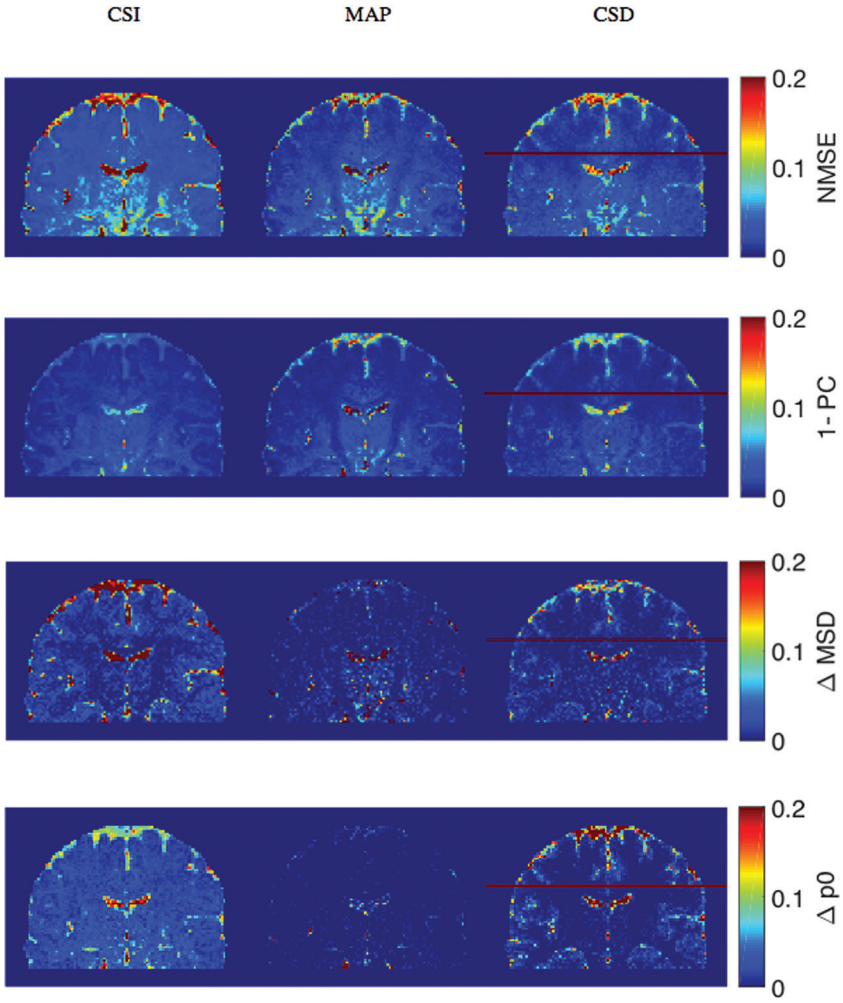

Fig. 4 Index-based maps from *in vivo* reconstructions for an undersampling factor of 4×. The first row corresponds to the NMSE maps; the second row to (1-PC) maps; the third row to relative MSD error maps; the fourth row to relative $p0$ error maps. The columns are the reconstruction methods: CSI, MAP and CSD. From the NMSE and (1-PC) maps, all methods are very similar and show reconstruction errors below 5%, except in areas containing cerebrospinal fluid or areas deeper in the brain. The real difference comes on the estimation of diffusion indices, where MAP shows more accuracy in recovering the MSD and $p0$ indices. CSI reconstruction provides the worst recovery, but its error is around 5% only. NMSE, normalized mean squared error; PC, Pearson Correlation Coefficient; MSD, mean squared displacement; $p0$, return to zero probability; CSI, Compressed Sensing using Identity; MAP, Mean Apparent Propagator; CSD, Compressed Sensing using Dictionary.

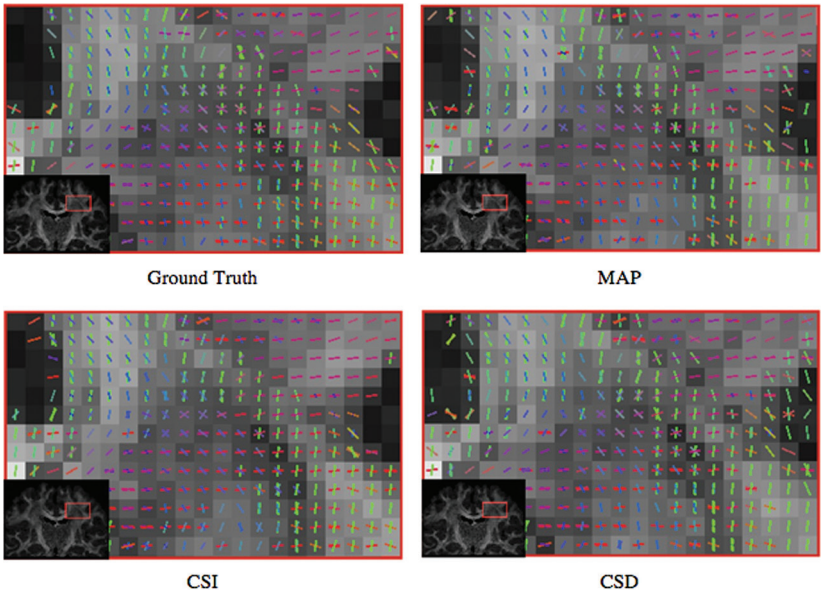

Fig. 5 Generalized fractional anisotropy maps from the ground truth and the reconstruction methods under investigation. From each map, we zoomed the region around the centrum semiovale for visual inspection of the directional information from the propagators obtained for those voxels. All methods show high similarity with the ground truth, but there are areas where directional information has errors (see for example the upper left corner of the zoomed areas). CSI, Compressed Sensing using Identity; MAP, Mean Apparent Propagator; CSD, Compressed Sensing using Dictionary.

(mean squared error and PC coefficient) and in terms of relative error metrics for propagator-based indices (ΔMSD and Δp0). The novelty of this comparison is that we included MAP in addition to CSD and CSI methods, which were previously analyzed.[19,20] The three reconstruction methods are representative of three classes: one method is based on fitting q-space signal to a highly efficient set of continuous basis functions; and two CS-based methods that sparsely encode the diffusion propagator by means of a sparsifying transform or by a dictionary constructed from the same measurements. We included in the simulations different reconstruction settings of noise, USF and crossing angles. In this way, we provided a thorough analysis to determine the advantages and limitations for the different methods; and complement the previous work. Our study has the same spirit as Hutchinson et al.,[34] but applied to reconstruction methods using Cartesian data with high q-space samples. Across the experiments, we observed that the Cartesian nature of the acquisition could influence the reconstruction of the directional information from diffusion MRI, so sampling patterns should be designed as isotropic as possible, taking this fact into consideration as in Paquette et al.[20] and Tobisch et al.[35]

In simulations, the CS reconstruction using data-driven sparse dictionary provided better results for the different settings and data when compared with MAP or CSI. Quantitatively speaking, MAP and CSI obtained 10% and 50% higher NMSE as compared with CSD. The observed reconstruction quality from the three reconstruction methods did not affect in a significant manner the estimation of propagator-based diffusion indices. The extraction of MSD and p0 were quite stable for different noise levels and crossing angles; nonetheless, MAP and CSI deviated from the ground truth, in both reconstruction quality and extraction of the propagator-based diffusion indices, at USF above 4×. Hutchinson et al.[34] justifies similar behavior on its results due to sampling dependency mainly, but in these experiments it may be more likely that the requirements for a robust optimization were not met for those USF and the reconstruction error propagated to the diffusion indices.

In the *in vivo* data, the reconstruction errors from the three methods at USF = 4 were below 5–8%, although MAP was the best; followed by CSD reconstruction and then CSI. Furthermore, MAP reconstruction gave higher quality in the extraction of propagator-based diffusion indices. The superior extraction of diffusion indices from MAP could be important if the objective of the study is related to the characterization of microstructure.

Mean apparent propagator[22] is a set of basis functions where the first basis function corresponds to Gaussian diffusion (DTI) and the extra basis functions are used to characterize non-Gaussian diffusion. In that sense, the method increases its accuracy for non-Gaussian diffusion by adding more basis functions. However, there is a condition in that the number of q-space samples must be enough to allow an appropriate reconstruction for that number of basis functions. Another factor affecting the reconstruction is the proper estimation of the diffusion tensor that scales the set of basis functions. This work reports that MAP using 50 basis functions worked well in terms of reconstruction quality and for recovering the propagator-based indices at low USF.

CSI reconstruction corresponds to the application of CS theory in diffusion spectrum imaging to reconstruct the diffusion propagator from a lower number of q-space samples than the sampling dictated by the Nyquist criterion. This work reports that CSI worked very similar when compared with MAP and CSD, but there was a consistently higher error at realistic noise levels. Although results from CSI reconstruction could change by the selection of another sparsifying transform or the value of the Lagrangian multiplier, in our experiments the identity was enough. This is confirmed since our results were similar to the results obtained in Bilgic

et al.[19] where they used wavelets and total variation as sparsifying transforms. Furthermore, in Paquette et al.[20] and Tobisch et al.[36] it is shown that it produces satisfactory reconstruction performance in comparison to other sparsifying transforms or methods based on other continuous basis functions.

Compressed sensing using data-driven dictionaries is a CS-based reconstruction procedure that assures the sparsity requirement in CSI theory using an ideal sparse dictionary constructed from the same measurements by means of the KSVD algorithm. Additionally, it provides an iterative parameter-free reconstruction method. This work reports that CSD showed higher reconstruction quality of the diffusion propagator and in the extraction of propagator-based diffusion indices. The effectiveness of CSD reconstruction is related to the quality of the data used for training. In simulations, the training was done with single fibers of different geometrical properties and rotated across the entire PDF-space without adding noise. This corresponds to an idealized complete training set for characterizing multiple fibers as a linear combination of single fibers. In the *in vivo* data, it is difficult to assure how rich or representative the slice used for training the dictionary was. The observed differences of propagator-based index errors between simulations and *in vivo* CSD reconstruction may be related to a lack of such training data richness. Another reason may be the fact that the training data for simulations was noise-free and the acquired *in vivo* data was not. Finally, it is difficult to establish which dictionary should be used if the specific parameters of the acquisition are not known. Furthermore, the dictionary could change across healthy and patient populations, or across age groups Bilgic et al.[19] One alternative is concatenating dictionaries from different acquisition schemes or objective-designed dictionaries. Nevertheless, there should not be major differences in the atoms between patients and healthy subjects. We expect the dictionaries to be complete enough to cover both populations. The differences should manifest more in the quantity and type of atoms chosen for each.

Future work could include further propagator-based quality measures, such as the non-Gaussianity[36] and the angular error in crossing angle[36] to complement NMSE, PC, MSD, and $p0$; to increase the characterization of the propagator reconstruction quantitatively. Finally, this comparison could be improved using recent advances of the corresponding methods, like the Laplacian regularized MAP,[24] joint k–q reconstruction,[37] or the implementation of deep learning for CSD like in Rasmussen et al.[38]

Conclusion

A comparison of different q-space reconstruction methods for undersampled diffusion spectrum imaging data was presented. The methods compared were MAP, CSI and CSD. The novelty of this comparison is that we included MAP in addition to CSD and CSI methods, to compare a method based on an efficient set of continuous basis functions with methods which are based on compressed sensing. Although all reconstruction methods worked well finding propagator-based indices, CSD was the best method for reconstructing the diffusion propagator from undersampled data. On the other hand, MAP results were more accurate in propagator-based diffusion indices at low USF.

Appendix A. Selection of Tuning Parameter for Compressed Sensing

CSI is the only method from the comparison that needs to tune a parameter (λ); and which may vary depending on the acquired data. To use Eq. [A.1],

$$\hat{p}(\boldsymbol{r}) = \operatorname{argmin}_{p(r)} \frac{1}{2}\left\|SFp(\boldsymbol{r}) - E(\mathbf{q})\right\|_2^2 + \lambda\left\|\Omega\, p(\boldsymbol{r})\right\|_1, \quad [A.1]$$

we applied two different heuristics:

Simulations

First, we analyzed the *l*-curve to obtain the λ that had a good balance between data consistency and the sparsity regularization. Second, we defined a threshold based on the NMSE in which the reconstruction error should be <5% error with regard to the ground truth. λ was changed until this was satisfied or the maximum number of iterations was exceeded. The maximum number of iterations was 6.

In vivo *data*

We repeated the heuristic from simulations on certain voxels along the coronal slice. Because the λ parameter was similar across the slice, we took the mean value from λs and applied it to the complete slice.

Appendix B. Evaluation of the Sampling Pattern

We evaluated 10 different sampling patterns with variable density distribution to analyze whether the behavior of the reconstruction quality was influenced by them. Figure 6 shows the results of the NMSE with respect to noise for the different patterns. The eighth pattern is not included here since it is the one used in the main document. Figure 7 shows the differences in reconstruction errors between sampling patterns specified in the rows and columns, $(\mathrm{NMSE}_{\mathrm{column}} - \mathrm{NMSE}_{\mathrm{row}})^2 / \mathrm{NMSE}^2_{\mathrm{row}}$. From the three methods, the CSD method shows more similar results across the different patterns (Fig.7c).

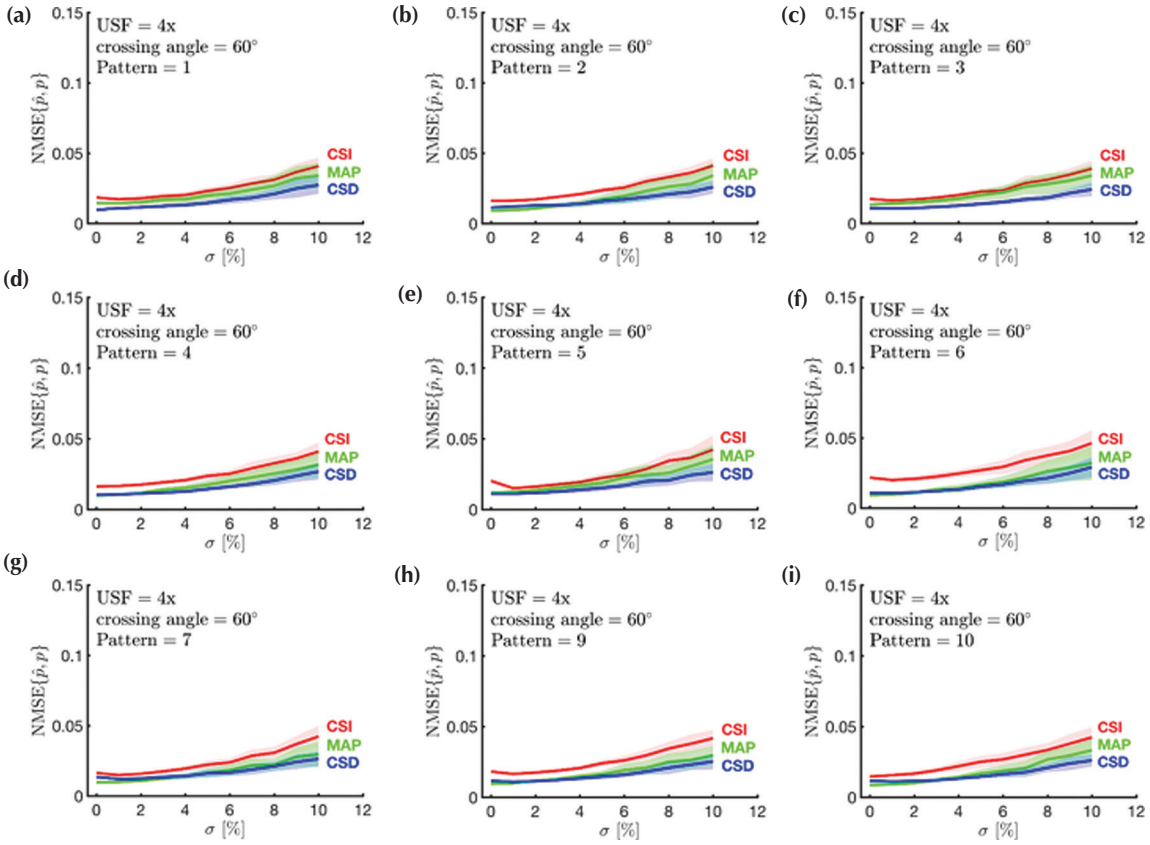

Fig. 6 (**a–i**) NMSE as a function of noise level σ for nine different sampling patterns. NMSE, normalized mean squared error; USF, undersampling factor; CSI, Compressed Sensing using Identity; MAP, Mean Apparent Propagator; CSD, Compressed Sensing using Dictionary.

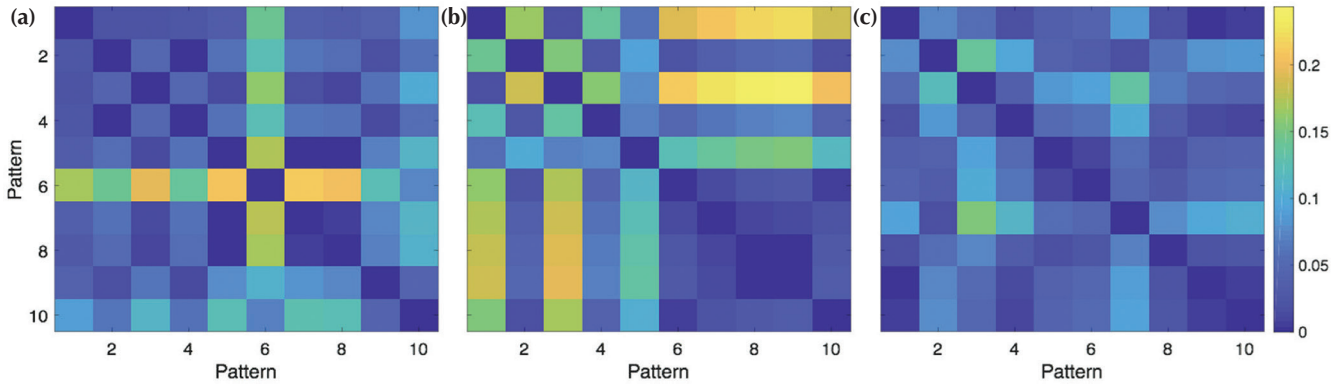

Fig. 7 NMSE difference matrix of the reconstruction methods. The colors indicate how much was the difference in reconstruction quality between the sampling patterns in the rows and columns of the matrix. Panel (**a**) corresponds to the NMSE difference matrix from CSI reconstruction; panel (**b**) from MAP reconstruction; and panel (**c**) from Compressed Sensing using Dictionary (CSD) reconstruction. NMSE, normalized mean squared error; CSI, Compressed Sensing using Identity.

Appendix C. *In vivo* Spatial Maps of NMSE for CSI, MAP and CSD Reconstructions at Different Undersampling Factors

Figure 8 shows the spatial maps of NMSE for the three reconstruction methods using USF = 4–6, and 8; as a way to validate how is the behavior of the reconstruction process in the *in vivo* data as the USF was increased.

Funding

The authors gratefully acknowledge CONICYT for funding this research through PIA-Anillo ACT1416 and scholarship CONICYT-PCHA/Doctorado-Nacional/2014-21140344; and Millenium Science Initiative of the Ministry of Economy, Development and Tourism, grant Nucleus for Cardiovascular Magnetic Resonance.

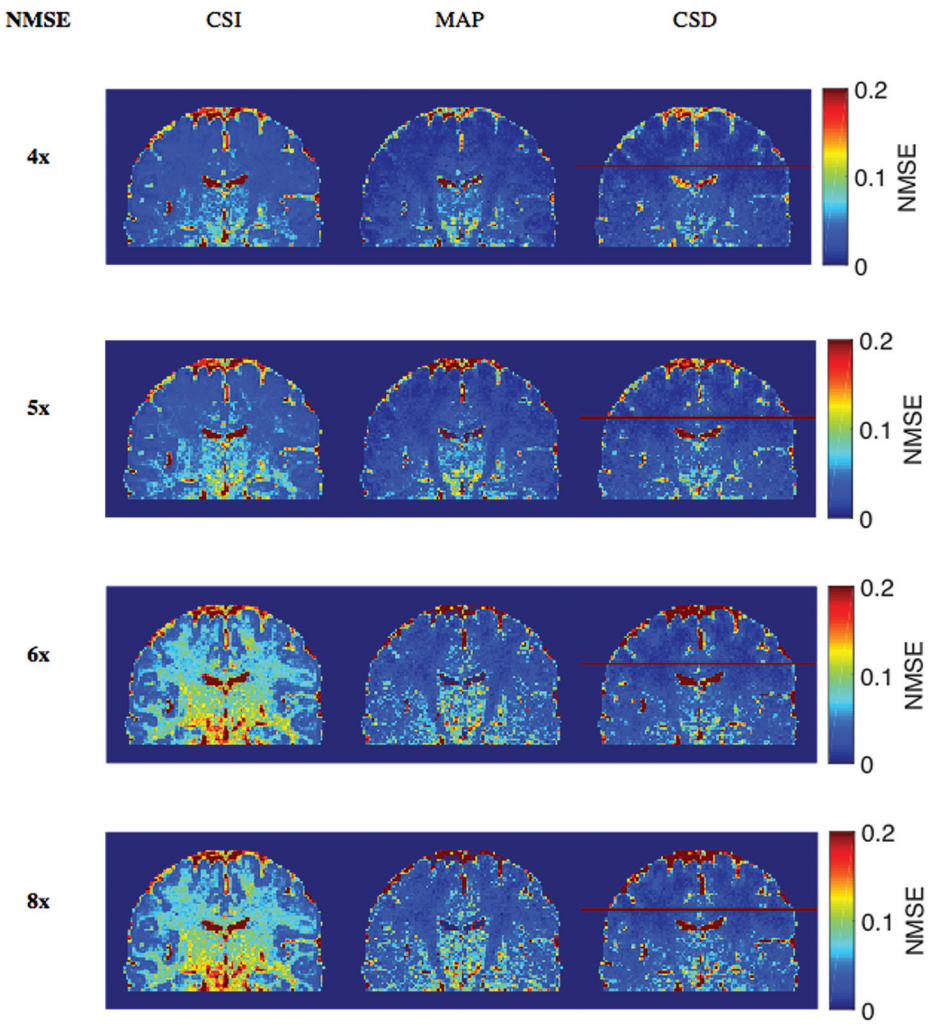

Fig. 8 NMSE spatial maps for CSI, MAP and CSD reconstruction methods at undersampling factors (USF) of 4×, 5×, 6×, and 8×. The spatial maps showed how CSD reconstruction preserved the reconstruction quality at higher USFs. NMSE, normalized mean squared error; CSI, Compressed Sensing using Identity; MAP, Mean Apparent Propagator; CSD, Compressed Sensing using Dictionary.

Conflicts of Interest

The authors declare that they have no conflicts of interest.

References

1. Callaghan PT. The measurement of motion using spin echoes. In Principles of Nuclear Magnetic Resonance Microscopy. New York: Oxford University Press 1991, 338–341.
2. Stejskal EO, Tanner JE. Spin diffusion measurements: spin echoes in the presence of a time-dependent field gradient. J Chem Phys 1965; 42:288–292.
3. Mitra PP, Halperin BI. Effects of finite gradient-pulse widths in pulsed field-gradient diffusion measurements. J Magn Reson A 1995; 113:94–101.
4. Wedeen VJ, Reese TG, Tuch DS, et al. Mapping fiber orientation spectra in cerebral white matter with fourier-transform diffusion MRI. Proceedings of the 8th Annual Meeting of ISMRM Denver, 2000; 82.
5. Wedeen VJ, Hagmann P, Tseng WY, Reese TG, Weisskoff RM. Mapping complex tissue architecture with diffusion spectrum magnetic resonance imaging. Magn Reson Med 2005; 54:1377–1386.
6. Lacerda LM, Sperl JI, Menzel MI, Sprenger T, Barker GJ, Dell'Acqua F. Diffusion in realistic biophysical systems can lead to aliasing effects in diffusion spectrum imaging. Magn Reson Med 2016; 76:1837–1847.
7. Paquette M, Gilbert G, Descoteaux M. Optimal DSI reconstruction parameter recommendations: better ODFs and better connectivity. Neuroimage 2016; 142:1–13.
8. Tian Q, Rokem A, Folkerth RD, et al. Q-space truncation and sampling in diffusion spectrum imaging. Magn Reson Med 2016; 76:1750–1763.
9. Basser PJ, Mattiello J, LeBihan D. MR diffusion tensor spectroscopy and imaging. Biophys J 1994; 66: 259–267.
10. Le Bihan D, Mangin JF, Poupon C, et al. Diffusion tensor imaging: concepts and applications. J Magn Reson Imaging 2001; 13:534–546.
11. Dong Q, Welsh RC, Chenevert TL, et al. Clinical applications of diffusion tensor imaging. J Magn Res Imaging 2004; 19:6–18.
12. Landman BA, Bogovic JA, Wan H, El Zahraa ElShahaby F, Bazin PL, Prince JL. Resolution of crossing fibers with constrained compressed sensing using diffusion tensor MRI. Neuroimage 2012; 59:2175–2186.

13. Jensen JH, Helpern JA, Ramani A, Lu H, Kaczynski K. Diffusional kurtosis imaging: the quantification of non-gaussian water diffusion by means of magnetic resonance imaging. Magn Reson Med 2005; 53:1432–1440.
14. Hagmann P, Jonasson L, Maeder P, Thiran JP, Wedeen VJ, Meuli R. Understanding diffusion MR imaging techniques: from scalar diffusion-weighted imaging to diffusion tensor imaging and beyond. Radiographics 2006; 26 Suppl 1: S205–S223.
15. Assemlal HE, Tschumperlé D, Brun L, Siddiqi K. Recent advances in diffusion MRI modeling: angular and radial reconstruction. Med Image Anal 2011; 15:369–396.
16. Ferizi U, Schneider T, Panagiotaki E, et al. A ranking of diffusion MRI compartment models with in vivo human brain data. Magn Reson Med 2014; 72:1785–1792.
17. Candès E, Romberg J. Sparsity and incoherence in compressive sampling. Inverse Problems 2007; 23:969–985.
18. Menzel MI, Tan ET, Khare K, et al. Accelerated diffusion spectrum imaging in the human brain using compressed sensing. Magn Reson Med 2011; 66:1226–1233.
19. Bilgic B, Setsompop K, Cohen-Adad J, Yendiki A, Wald LL, Adalsteinsson E. Accelerated diffusion spectrum imaging with compressed sensing using adaptive dictionaries. Magn Reson Med 2012; 68:1747–1754.
20. Paquette M, Merlet S, Gilbert G, Deriche R, Descoteaux M. Comparison of sampling strategies and sparsifying transforms to improve compressed sensing diffusion spectrum imaging. Magn Reson Med 2015; 73:401–416.
21. Merlet S. Compressive sensing in diffusion MRI. Université Nice Sophia Antipolis, 2013; NNT : 2013NICE4061. tel-00908369v2.
22. Özarslan E, Koay CG, Shepherd TM, et al. Mean apparent propagator (MAP) MRI: a novel diffusion imaging method for mapping tissue microstructure. Neuroimage 2013; 78:16–32.
23. Avram AV, Sarlls JE, Barnett AS, et al. Clinical feasibility of using mean apparent propagator (MAP) MRI to characterize brain tissue microstructure. Neuroimage 2016; 127:422–434.
24. Fick RHJ, Wassermann D, Caruyer E, Deriche R. MAPL: Tissue microstructure estimation using Laplacian-regularized MAP–MRI and its application to HCP data. Neuroimage 2016; 134:365–385.
25. Cook PA, Bai Y, Nedjati-Gilani S, et al. Camino: Open-source Diffusion-MRI Reconstruction and Processing. Proceedings of the 14th Annual Meeting of the ISMRM, Seattle, 2006; 2759.
26. Hall MG, Alexander DC. Convergence and parameter choice for Monte-Carlo simulations of diffusion MRI. IEEE Trans Med Imaging 2009; 28:1354–1364.
27. Tobisch A, Stirnberg R, Harms RL, et al. Compressed sensing diffusion spectrum imaging for accelerated diffusion microstructure MRI in long-term population imaging. Front Neurosci 2018; 12:650. doi:10.3389/fnins.2018.00650
28. Andersson JL, Skare S, Ashburner J. How to correct susceptibility distortions in spin-echo echo-planar images: application to diffusion tensor imaging. Neuroimage 2003; 20:870–888.
29. Andersson JL, Sotiropoulos SN. Non-parametric representation and prediction of single- and multi-shell diffusion-weighted MRI data using Gaussian processes. Neuroimage 2015; 122:166–176.
30. Aharon M, Elad M, Bruckstein A. *rm* K-SVD: an algorithm for designing overcomplete dictionaries for sparse representation. IEEE Trans Signal Process 2006; 54: 4311–4322.
31. Ye JC, Tak S, Han Y, Park HW. Projection reconstruction MR imaging using FOCUSS. Magn Reson Med 2007; 57:764–775.
32. Wu YC, Field AS, Alexander AL. Computation of diffusion function measures in q-space using magnetic resonance hybrid diffusion imaging. IEEE Trans Med Imaging 2008; 27:858–865.
33. Assaf Y, Mayk A, Cohen Y. Displacement imaging of spinal cord using q-space diffusion-weighted MRI. Magn Reson Med 2000; 44:713–722.
34. Hutchinson EB, Avram AV, Irfanoglu MO, et al. Analysis of the effects of noise, DWI sampling, and value of assumed parameters in diffusion MRI models. Magn Reson Med 2017; 78:1767–1780.
35. Tobisch A, Varela G, Stirnberg R, et al. Sparse isotropic q-space sampling distribution for compressed sensing in DSI. Proceedings of the 22nd Annual Meeting of ISMRM, Milan, 2014; 4451.
36. Tobisch A, Schultz T, Stirnberg R, et al. Comparison of basis functions and q-space sampling schemes for robust compressed sensing reconstruction accelerating diffusion spectrum imaging. NMR Biomed 2019; 32:e4055. doi:10.1002/nbm.4055.
37. Sun J, Sakhaee E, Entezari A, Vemuri BC. Leveraging EAP-sparsity for compressed sensing of MS-HARDI in (k,q)-space. In: Ourselin S, Alexander DC, Westin C-F, Cardoso MJ. eds. Information Processing in Medical Imaging, 24th International Conference, IPMI 2015, Springer International Publishing, USA, 2015; 375-386
38. Rasmussen KGB, Kristensen M, Blendal RG, et al. DeepQSM - using deep learning to solve the dipole inversion for MRI susceptibility mapping. BioRxiv, 2018. doi:10.1101/278036